2023 24th International Carpathian Control Conference (ICCC) | 979-8-3503-1022-1/23/$31.00 ©2023 IEEE | DOI: 10.1109/ICCC57093.2023.10178963

Cascade MIMO P-PID Controllers Applied in an Over-actuated Quadrotor Tilt-Rotor

Murillo Ferreira dos Santos
Department of Electroelectronics,
CEFET-MG, Leopoldina, Brazil
murillo.ferreira@cefetmg.br

Leonardo de Mello Honório
Department of Energy
Juiz de Fora Federal University, Brazil
leonardo.honorio@ufjf.edu.br

Mathaus Ferreira da Silva
Department of Energy
Juiz de Fora Federal University, Brazil
mathaus.silva@engenharia.ufjf.br

William Rodrigues Silva
Department of Electroelectronics,
CEFET-MG, Leopoldina, Brazil
williamrsilva97@gmail.com

José Luís Sousa de Magalhães Lima
Instituto Politécnico de Bragança, IPB,
Research Centre in Digitalization and
Intelligent Robotics (CeDRI), Bragança
Portugal jllima@ipb.pt

Paolo Mercorelli
Institute for Production Technology
and Systems (IPTS) Leuphana University
of Lüneburg, Lüneburg, Germany
paolo.mercorelli@leuphana.de

Marlon José do Carmo
Department of Electroelectronics,
CEFET-MG, Leopoldina, Brazil
marlon@cefetmg.br

***Abstract*—To map the Virtual Control Actions (VCAs) into Real Control Actions (RCAs), over-actuated systems typically require nonlinear control allocation methods. On embedded robotic platforms, computational efforts are not always available. With this in mind, this work presents the design of a Quadrotor Tilt-Rotor (QTR) through a new concept of control allocation with uncoupled RCAs, where a nonlinear system is divided into partially dependent and linear subsystems with fast and robust convergence. The RCAs are divided into smaller and linearized sets and solved sequentially. Then, the cascade Multipe-Input-Multipe-Output (MIMO) Proportional (P)-Proportional, Integral and Derivative (PID) controllers tuning were presented with saturation constants and successive loop closure technique, where some open-field environment tests were conducted to validate the respective tuning. In the end, it showed to be reliable, robust, efficient, and applicable when VCAs are overlapped between the subsystems.**

***Index Terms*—P-PID Controller, Overactuated Vehicle, MIMO Cascade Controller**

I. INTRODUCTION

As suggested by the name, the Unmanned Aerial Vehicles (UAVs) are vehicles able to move through the air without close human interference or even totally autonomous, popularly known as drones. Through their overfly ability, these vehicles can supervise dangerous and/or inaccessible areas [1]. According to the United States Federal Aviation Administration (FAA), more than 1 million UAVs have been registered until September 2018 in the last few years [2].

The control of those vehicles is essential to avoid collisions, but non-linear flight dynamics are a challenge due to real-time control needed to maintain stability [3]. On this, a usual control method observed is the Non-Linear Dynamic Inversion (NDI), widely applied in flight control as can be observed in the works [4], [5]. Another one commonly observed in recent works can be applied in UAVs for the Fault-Tolerance Control (FTC), such as presented in [6].

Furthermore, the UAV control in open-field is indispensable as long it requires precision to deal with multiple wings, flight resistance and the vehicle weight [7].

Some important works can be highlighted, such as [4], where it was applied the hybrid NDI based on the angular acceleration feedback control to improve the system robustness and performance joining the NDI and INDI (Incremented NDI) attributes: feedforward control, proportional control, and logical integral control. These results demonstrate the robustness and excellence of this method. In the hybrid NDI control method, good control results can be attributed mainly to feedback control of the angular acceleration signals because it eliminates system uncertainties, nonlinearities, couplings, and time-varying problems.

In [6] is observed the appliance of the FTC focused on the faulty fixed-wing with the errors provided to the actuators. After, it is detected and transformed into a new set of variables to compensate the fault and keep the UAV working safely.

Based on this, the present work aims to detail the cascade MIMO P-PID controller with its respective tuning, applied to the overactuated QTR UAV developed in [8], [9]. The aircraft topology is in H form and its RCAs are totally independent through Fast Control Allocation (FCA) technique. For this purpose, it is also presented a safe testing environment to analyze the QTR angular stability before the open-field experiments.

This work is divided as follows: Section II presents the QTR kinematics and dynamics modeling which will bring some basic notions of its constructive part and the description

978-8-3503-1022-1/23/$31.00 ©2023 IEEE

of its actuators; Section III presents the QTR overall control structure, providing a detailed explanation of the entire control loop, also depicting the control allocation, named as FCA; Section IV demonstrate how the cascade MIMO P-PID are tuned; Section IV presents some experimental results: in the gyroscopic testbench and in open-field. In the end, Section VI concludes the work with some future works.

II. QTR KINEMATICS AND DYNAMICS MODELLING

The aircraft is flying over a small area of the planet, which implies that the radius of the Earth tends to infinity, so the centripetal acceleration of the curvature is ignored.

The UAV kinematics behavior is described by twelve state variables: p_n (inertial position (north) along $\hat{\boldsymbol{i}}^i$ in $\mathcal{F}^i$; p_c (inertial position (east) along $\hat{\boldsymbol{j}}^i$ in $\mathcal{F}^i$); h (height measured along $\hat{\boldsymbol{k}}^i$ in $\mathcal{F}^i$); u (velocity measured along $\hat{\boldsymbol{i}}^b$ in $\mathcal{F}^b$); v (velocity measured along $\hat{\boldsymbol{j}}^b$ in $\mathcal{F}^b$); ω (velocity measured along $\hat{\boldsymbol{k}}^b$ in $\mathcal{F}^b$); ϕ (roll angle relative to $\mathcal{F}^{v2}$); θ (pitch angle relative to $\mathcal{F}^{v1}$); ψ (yaw angle relative to $\mathcal{F}^v$); p (roll rate measured over $\hat{\boldsymbol{i}}^b$ in $\mathcal{F}^b$); q (pitch rate measured over $\hat{\boldsymbol{j}}^b$ in $\mathcal{F}^b$); r (yaw rate measured over $\hat{\boldsymbol{k}}^b$ in $\mathcal{F}^b$).

The UAV translation velocity is commonly determined by the frame that joins the drone's structure [10], [11]. The components $u, v,$ and ω correspond to the inertial velocities [12]. Equations (1) and (2) describe those positions and their speeds.

$$\frac{d}{dt}\begin{bmatrix} p_n \\ p_e \\ -h \end{bmatrix} = \boldsymbol{A}_v^b \begin{bmatrix} u \\ v \\ \omega \end{bmatrix} = (\boldsymbol{A}_b^v)^T \begin{bmatrix} u \\ v \\ \omega \end{bmatrix}, \tag{1}$$

$$(\boldsymbol{A}_b^v)^T = \begin{bmatrix} c\theta c\psi & s\phi s\theta c\psi - c\theta s\psi & c\phi s\theta c\psi + s\phi s\psi \\ c\theta s\psi & s\phi s\theta s\psi + c\phi c\psi & c\phi s\theta s\psi - s\phi c\psi \\ -s\theta & s\phi s\theta & c\phi c\theta \end{bmatrix} \tag{2}$$

The angles $\phi, \theta,$ and ψ are positioned in different frames from the other ones, which implies using rotational matrix [12], [13] resultin in the matrices in (3):

$$\begin{bmatrix} p \\ q \\ r \end{bmatrix} = \begin{bmatrix} 1 & 0 & -s\theta \\ 0 & c\phi & s\phi c\theta \\ 0 & -s\phi & c\phi c\theta \end{bmatrix} \begin{bmatrix} \dot{\phi} \\ \dot{\theta} \\ \dot{\psi} \end{bmatrix}. \tag{3}$$

Evidencing the angular positions, (3) turns into (4).

$$\begin{bmatrix} \dot{\phi} \\ \dot{\theta} \\ \dot{\psi} \end{bmatrix} = \begin{bmatrix} 1 & s\phi t\theta & c\phi t\theta \\ 0 & c\theta & -s\phi \\ 0 & s\phi/c\theta & c\phi/c\theta \end{bmatrix} \begin{bmatrix} p \\ q \\ r \end{bmatrix}. \tag{4}$$

The dynamics modeling is divided into translational and rotational, both following Newton's Second Law [12].

Starting with the translational part, based on the linear momentum conservation equations, (5) shows the relations since Newton's Second law until letting it in the function of the QTR mass m, the velocity vector v through $\boldsymbol{i^b}, \boldsymbol{j^b}$ and $\boldsymbol{k^b}$ and the vector f which means the summation of the all external forces (gravitational, aerodynamic and propulsion).

$$\begin{gathered} \boldsymbol{f} = m\bar{\boldsymbol{a}}, \\ m\frac{d\boldsymbol{v}}{dt_i} + \boldsymbol{v}\frac{dm}{dt_i} = \boldsymbol{f}. \end{gathered} \tag{5}$$

As the mass does not change with time, (5) is reduced to (7) whose derivative is in time on the inertial frame $\mathcal{F}^i$.

$$m\frac{d\boldsymbol{v}}{dt_i} = \boldsymbol{f}. \tag{6}$$

The derivative of the velocity in the inertial frame can be described in terms of the derivative of frame $\mathcal{F}^b$ joined to the structure and the angular velocity reaching in (7), (8) and (9).

$$\frac{d\boldsymbol{v}}{dt_i} = \frac{d\boldsymbol{v}}{dt_b} + \boldsymbol{\omega}_{\boldsymbol{b/i}} \times \boldsymbol{v}, \tag{7}$$

$$m\left[\frac{d\boldsymbol{v}}{dt_b} + \boldsymbol{\omega}_{\boldsymbol{b/i}} \times \boldsymbol{v}\right] = \boldsymbol{f}, \tag{8}$$

$$m\left[\frac{d\boldsymbol{v}^b}{dt_b} + \boldsymbol{\omega}_{\boldsymbol{b/i}} \times \boldsymbol{v}^b\right] = \boldsymbol{f}^b. \tag{9}$$

Knowing that $\frac{d\mathbf{v}^b}{dt_b}$ is the derivative of the frame $\mathcal{F}^b$ joined to the structure, it is equal to the vector of derivatives of the velocities u, v and ω described at the beginning of this section.

Now, rewriting the cross product from (9), it reaches in (10).

$$\boldsymbol{\omega}_{\boldsymbol{b/i}} \times \boldsymbol{v}^b = \boldsymbol{i^b}\left(q\omega - rv\right) + \boldsymbol{j^b}\left(ur - p\omega\right) + \boldsymbol{k^b}\left(pv - qu\right). \tag{10}$$

Then, keeping in mind that $\boldsymbol{i^b}, \boldsymbol{j^b}$ and $\boldsymbol{k^b}$ are unit vectors and considering the respective axes forces, the translation can be described in (11).

$$\boldsymbol{\omega}^{\boldsymbol{b}}_{\boldsymbol{b/i}} \times \boldsymbol{v}^b = \begin{bmatrix} \dot{u} \\ \dot{v} \\ \dot{\omega} \end{bmatrix} = \begin{bmatrix} rv - q\omega \\ p\omega - ur \\ qu - pv \end{bmatrix} + \frac{1}{m}\begin{bmatrix} X_p^b \\ Y_p^b \\ Z_p^b \end{bmatrix}. \tag{11}$$

where X_p^b, Y_p^b and Z_p^b are the resultant forces for rolling, pitching and yawing, respectively on the fixed-body frame.

About the rotational movement, the Second's Newton Law turns into (12):

$$\frac{d\boldsymbol{H^b}}{dt_i} + \boldsymbol{\omega}^{\boldsymbol{b}}_{\boldsymbol{b/i}} \times \boldsymbol{H}^b = \boldsymbol{t^b}. \tag{12}$$

In rigid structures, the angular momentum is defined by the product between the inertia matrix $\boldsymbol{J}^b \in \mathbb{R}^{3x3}$ and the angular vector $\boldsymbol{H}^b = \boldsymbol{J}^b\boldsymbol{\omega}^b_{b/i}$ where $\mathbb{R}^{3x3}$ is defined in (13).

$$\boldsymbol{J^b} = \begin{bmatrix} J_x & -J_{xy} & -J_{xz} \\ -J_{xy} & J_y & -J_{yz} \\ -J_{xz} & -J_{yz} & J_z \end{bmatrix}. \tag{13}$$

The integrals presented in (13) were calculated in function of the axes $\boldsymbol{i^b}, \boldsymbol{j^b}$ and $\boldsymbol{k^b}$ in $\mathcal{F}^b$, where the inertia momentum J^b is considered constant seen from the same frame, which implies $\frac{d\boldsymbol{J^b}}{dt_b} = 0$ [14]. Then, (12) turns into (14):

$$\boldsymbol{J^b}\frac{d\boldsymbol{\omega}^{\boldsymbol{b}}_{\boldsymbol{b/i}}}{dt_b} + \boldsymbol{\omega}^{\boldsymbol{b}}_{\boldsymbol{b/i}} \times \boldsymbol{J}^b\boldsymbol{\omega}^{\boldsymbol{b}}_{\boldsymbol{b/i}} = \boldsymbol{t^b}. \tag{14}$$

The angular velocity can be written in terms of the derivative matrix of the instantaneous projections on the $\boldsymbol{i^b}, \boldsymbol{j^b}$ and $\boldsymbol{k^b}$ of the roll, pitch and yaw rate measure p, q and r, respectively. Isolating the angular velocity of (14), (15) appears.

$$\begin{bmatrix} \dot{p} \\ \dot{q} \\ \dot{r} \end{bmatrix} = \boldsymbol{J^{b^{-1}}} \left(- \begin{bmatrix} \dot{p} \\ \dot{q} \\ \dot{r} \end{bmatrix} \times \boldsymbol{J^b} \begin{bmatrix} \dot{p} \\ \dot{q} \\ \dot{r} \end{bmatrix} + \begin{bmatrix} L_p^b \\ M_p^b \\ N_p^b \end{bmatrix} \right), \tag{15}$$

where L_p^b, M_p^b and N_p^b are the resultant torques for rolling, pitching and yawing, respectively on the fixed-body frame.

Then, the 6 DoFs from Newton-Euler modeling for UAV kinematics and dynamics is described by (1), (4), (11) and (15).

III. QTR OVERALL CONTROL STRUCTURE

Fig. 1 presents the control structure composed by the five inputs: roll, pitch, yaw, high and the linear velocity which result in the virtual controls that will be used to control the eight real variables that correspond to the actuators: γ_i and δ_i.

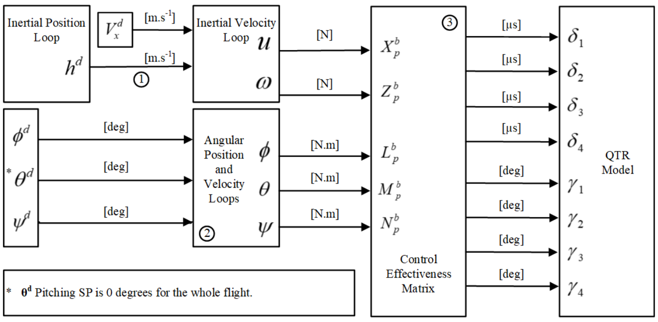

Fig. 1: QTR control structure

A. FCA Control Allocation

This control method is based on a faster linear version compared to the traditional linear approach described by dividing the problem into two subsets interconnected [8], [15].

In this way, the non-linear system can be divided into two different problems, as shown in (16) and (17).

$$\boldsymbol{\tau_a} = \boldsymbol{M_a}\left(\boldsymbol{u_b}\right)\boldsymbol{u_a}, \tag{16}$$

$$\boldsymbol{\tau_b} = \boldsymbol{M_b}\left(\boldsymbol{u_a}\right)\boldsymbol{u_b}, \tag{17}$$

where $\boldsymbol{u_a} \in \mathbb{R}$ with $q \in \mathbb{N}$ represents a part of the n system actuators, $\boldsymbol{u_b} \in \mathbb{R}^r$ with $r \in \mathbb{N}$ represents the remaining actuators, $\boldsymbol{\tau_a} \in \mathbb{R}^{m_a}$, $\boldsymbol{\tau_b} \in \mathbb{R}^{m_b}$, $\boldsymbol{M_a(u_a)} \in \mathbb{R}^{m_a \times q}$ and $\boldsymbol{M_b(u_b)} \in \mathbb{R}^{m_b \times q}$ which are the QTR sub-Control Effectiveness Matrixs (CEMs).

Then, the initial non-linear system can be described into two combinations:

- Separate the defined VCAs in which the resulting set generates two dependents and linear subsystems. It linearizes a set considering the previous action of the other one;
- The VCAs in the first subset should be completely overlapped on the second one aiming to facilitate its convergence. The absence or partiality overlapping cannot guarantee convergence in situations even with the desired signal is still reachable.

The non-linearities of the RCAs are divided into two independent problems that can be solved by a recursive and iterative form until reaching the convergence criteria.

IV. MIMO P-PI CONTROLLERS TUNING

The QTR control structure is run at a higher level than the allocation control marked with the number 3 shown in Fig. 1.

The control loop was implemented with an external cascade level using a P controller and an internal one with a PID.

Regarding the forward/backward velocity (V_x), it was created only one level through a PID controller, with the same frequency of the height velocity loop ($40Hz$).

Taking the tuning into account, it is designed according to the canonical transfer function shown in (18), where ξ is the damping coefficient and ω_n is the natural frequency chosen.

$$G(s) = \frac{\omega_n^2}{s^2 + 2\xi\omega_n + \omega_n^2}. \tag{18}$$

Considering the simplified model of all control loops, the methodology used in the works of [16]–[18] was followed.

A. Angular Position and Velocity Loops Tuning

When the angle is small or equal to zero, the amplitude of the controller action can be determined by the amplitude of the control error and proportional gain k_p. When $u^{max} = k_p e^{max}$, (19) can be used to get the proportional gain of the pitch angular position controller.

$$k_p^\theta = \frac{u^{max} - u^{min}}{e^{max} - e^{min}} = \frac{\Delta u}{\Delta e} = \frac{5 - (-5)}{2.5 - (-2.5)} = 2. \tag{19}$$

From (19), the considered maximum error Δe was 5 degrees, given that the vehicle was designed to remain at 0 degrees of pitch. As the output from the controller, the Δu adopted was 10 degrees/sec. For the proportional controller of angular roll attitude presented in (20).

$$k_p^\phi = \frac{10 - (-10)}{10 - (-10)} = \frac{20}{20} = 1.0. \tag{20}$$

In this controller, different from the pitch one, the QTR can receive setpoints different from 0 degrees, limited from -10 to $+10$ degrees at each iteration ($\Delta e = 20$ degrees). For the control action, $\Delta u = 20$ degrees/sec was considered.

For the yaw loop, a gain $k_p^\psi = 3.0$ was obtained.

For the rolling angular velocity loop, torque control actions were adopted with a minimum value of -1.1768 and a maximum of 1.1768 N, therefore, $\Delta u = 2.3536$ Nm. The maximum rolling velocity error comes from the control action of the rolling angular position loop, where $\Delta e = 20$ degrees/sec generating $k_p^{\dot{\phi}} = 0.1177$.

For the angular pitch velocity loop, $\Delta u = 2.3536$ Nm and $\Delta e = 10$ degrees/sec, resulting in $k_p^{\dot{\theta}}$ =0.23536.

Taking yawing into consideration, it was obtained that the servomotors will allow the QTR to generate a maximum torque close to 8.46 Nm with $\Delta u = 16.92$ Nm. For maximum yaw error, $\Delta e = 45$ degrees/sec was taken. Therefore, $k_p^{\dot{\psi}} = 0.376$.

Considering that vehicle's inertia matrix has only moments of inertia, the dynamics is reduced to (21), (22) and (23).

$$\dot{\phi}(s) = \frac{1}{J_x s} L_p^b(s), \tag{21}$$

$$\dot{\theta}(s) = \frac{1}{J_y s} M_p^b, \tag{22}$$

$$\dot{\psi}(s) = \frac{1}{J_z s} N_p^b. \tag{23}$$

However, the torques generated by the controllers must be distributed respectively to the 8 QTR actuators. To tune the controllers, the CEM constants must be grouped in the variables b_1, b_2 and b_3.

Manipulating the CEM presented in the works [8], [9] and applying the approximation for small angles ($\cos x \cong 1$ and $\sin x \cong x$), it reaches in (24), (25) and (26).

Considering that the value of the constant k_2 is negligible compared to that of k_1, it results in (27), (28) and (29):

Substituting the torques $L_p^b(s)$, M_p^b and N_p^b in (21), (22) and (23), the variables b_1, b_2 and b_3 are:

$$\dot{\phi}(s) = \frac{b_1}{s} \Delta\delta(s), \tag{30}$$

$$\dot{\theta}(s) = \frac{b_2}{s} \Delta\delta(s), \tag{31}$$

$$\dot{\psi}(s) = \frac{b_3}{s} \Delta\gamma\delta(s), \tag{32}$$

where $b_1 = \dfrac{k_1}{J_x}$; $b_2 = \dfrac{k_1}{J_y}$; $b_3 = \dfrac{k_1}{J_z}$; $\Delta\delta$ is the subtraction of the positive and negative terms of the propulsion motor RCAs; $\Delta\gamma\delta$ is the subtraction of the positive terms from the negative ones, where now each term is the product of a propulsion motor RCA by the respective servomotor RCA.

At the end of the angular velocity control actions, the closed-loop transfer functions are presented from (33) to (35):

$$\frac{\dot{\phi}(s)}{\dot{\phi}^d(s)} = \frac{b_1(k_d^{\dot{\phi}} s^2 + k_p^{\dot{\phi}} s + k_i^{\dot{\phi}})}{(1 + b_1 k_d^{\dot{\phi}})s^2 + b_1 k_p^{\dot{\phi}} s + b_1 k_i^{\dot{\phi}}}, \tag{33}$$

$$\frac{\dot{\theta}(s)}{\dot{\theta}^d(s)} = \frac{b_2(k_d^{\dot{\theta}} s^2 + k_p^{\dot{\theta}} s + k_i^{\dot{\theta}})}{(1 + b_2 k_d^{\dot{\theta}})s^2 + b_2 k_p^{\dot{\theta}} s + b_2 k_i^{\dot{\theta}}}, \tag{34}$$

$$\frac{\dot{\psi}(s)}{\dot{\psi}^d(s)} = \frac{b_3(k_d^{\dot{\psi}} s^2 + k_p^{\dot{\psi}} s + k_i^{\dot{\psi}})}{(1 + b_3 k_d^{\dot{\psi}})s^2 + b_3 k_p^{\dot{\psi}} s + b_3 k_i^{\dot{\psi}}}, \tag{35}$$

where $\dot{\phi}^d$, $\dot{\theta}^d$ and $\dot{\psi}^d$ are the respective desired rolling, pitching and yawing angular velocities, resulting from the angular position loop control action P.

Matching the characteristic polynomials of the functions presented above with the desired canonical function in (18) and considering $\zeta = 0.8$ and $w_n = 5$ rad/sec: $k_d^{\dot{\phi}} = 0.0017$, $k_i^{\dot{\phi}} = 0.3678$, $k_d^{\dot{\theta}} = 0.0020$, $k_i^{\dot{\theta}} = 0.7355$, $k_d^{\dot{\psi}} = 1.1750$ and 0.0196.

B. Inertial Position and Velocity Loops Tuning

With the angular dynamics stabilized, it is started the altitude h and speed V_x controllers tuning along the $\hat{\boldsymbol{\imath}}^{\boldsymbol{b}}$ axis.

First, the tuning of the proportional gain P for the altitude inertial position loop will be presented, and then the tuning of the inertial velocity control loops V_x and ω.

Again, it is considered the first-order approximation for small angles of terms involving cosine: $\cos x \cong 1$. The terms $\sin\theta$ were approximated to 0 because the vehicle is not rotated significantly in pitch.

Following the same methodology for obtaining the gains of the proportional controllers P of the low-level control loops, $\Delta e = 10$ m and $\Delta u = 5$ m/sec in each iteration, obtains (36).

$$k_p^h = \frac{2.5 - (-2.5)}{5 - (-5)} = \frac{5}{10} = 0.5, \tag{36}$$

where 2.5 m/sec is the climb rate.

For $k_p^{V_x}$ is considered the saturation limits on the thrust force for the servomotors tilting, ranging from -11.0950 to 11.0950 N. This generates $\Delta u = 22.19N$ as in (37) to (38).

$$SAT_P = 4gT_M = 15,6906N, \tag{37}$$

$$SAT_{V_x} = SAT_P \cos 45^o = 11,0950N, \tag{38}$$

where g is the acceleration due to gravity, $9.8066m/s^2$; SAT_P is the maximum force generated by the 4 propellers together; SAT_{V_x} is the maximum thrust force projected along the $\hat{\boldsymbol{\imath}}^{\boldsymbol{b}}$ axis; $T_M = 0.4Kg$ is the maximum thrust each engine is capable of producing.

Adopting $\Delta e = 5$ m/s, the proportional gain P of the speed controller V_x is expressed in (39).

$$k_p^{V_x} = \frac{11.095 - (-11.095)}{2.5 - (-2.5)} = 4.438. \tag{39}$$

For k_p^{ω}, the maximum actuation of the altitude inertial position controller (5 m/sec) becomes the maximum error of the velocity loop ω, being 2.5 m/sec for engines off (the maximum allowed speed that gravitational force can impart on the aircraft) and -2.5 m/sec for propulsion motors in operation.

The maximum performance in the ω velocity loop considered here was $u^{max} = -15.6906$ N for upward movements and $u^{min} = 9.8361$ N (engines off where only the force gravitational force acts), resulting in (40).

$$k_p^{\omega} = \frac{15.6906 - (-9,8361)}{2.5 - (-2.5)} = 5.1053. \tag{40}$$

Neglecting the Coriolis terms and applying the approximation for small angles ($\cos x \cong 1$ and $\sin x \cong x$), it is shown the simplified transfer functions of the velocity controllers.

$$L_p^b(s) = k_1[\delta_2(s)+\delta_3(s)-\delta_1(s)-\delta_4(s)] + k_2[\gamma_3(s)\delta_3(s)+\gamma_4(s)\delta_4(s)-\gamma_1(s)\delta_1(s)-\gamma_2(s)\delta_2(s)], \tag{24}$$

$$M_p^b = k_1[\delta_1(s)+\delta_3(s)-\delta_2(s)-\delta_4(s)], \tag{25}$$

$$N_p^b = k_1[\gamma_2(s)\delta_2(s)+\gamma_3(s)\delta_3(s)-\gamma_1(s)\delta_1(s)-\gamma_4\delta_4(s)] + k_2[\delta_1(s)+\delta_2(s)-\delta_3(s)-\delta_4(s)] \tag{26}$$

$$L_p^b(s) = k_1[\delta_2(s)+\delta_3(s)-\delta_1(s)-\delta_4(s)], \tag{27}$$

$$M_p^b = k_1[\delta_1(s)+\delta_3(s)-\delta_2(s)-\delta_4(s)], \tag{28}$$

$$N_p^b = k_1[\gamma_2(s)\delta_2(s)+\gamma_3(s)\delta_3(s)-\gamma_1(s)\delta_1(s)-\gamma_4\delta_4(s)]. \tag{29}$$

$$V_x(s) = \frac{X_p^b(s)}{ms}, \tag{41}$$

$$\omega(s) = \frac{g}{s} - \frac{Z_p^b(s)}{ms}. \tag{42}$$

Manipulating again the CEM presented in the works [8], [9], considering that the drag force is small compared to the QTR displacement force and applying again the approximation for small angles, (43) and (44) are obtained.

$$X_p^b(s) = k_1[\Delta\gamma\delta(s)], \tag{43}$$

$$Z_p^b(s) = -k_1[\sum_{i=1}^{4}\delta_i(s)]. \tag{44}$$

Substituting the forces X_p^b and Z_p^b in (41) and (42), it is obtained the closed-loop transfer functions for the inertial velocities V_x and ω in (45) and (46):

$$\frac{V_x(s)}{V_x^d(s)} = \frac{k_1(k_d^{V_x}s^2 + k_p^{V_x}s + k_i^{V_x})}{(m + k_1k_d^{V_x})s^2 + k_1k_p^{V_x}s + k_1k_i^{V_x}}, \tag{45}$$

$$\frac{\omega(s)}{\omega^d(s)} = \frac{k_1(k_d^{\omega}s^2 + k_p^{\omega}s + k_i^{\omega})}{(m + k_1k_d^{\omega})s^2 + k_1k_p^{\omega}s + k_1k_i^{\omega}}. \tag{46}$$

where V_x^d and ω^d are the respective desired inertial velocity setpoints V_x and ω.

Following the same methodology used in the angular velocity control and considering $\zeta = 0.9$, $w_n = 2.5$ rad/sec for both dynamics, the gains $k_i^{V_x} = 6.1639$, $k_i^{\omega} = 7.0907$, $k_d^{V_x} = 0.7305$ and $k_d^{\omega} = 0.8788$ are calculated.

V. EXPERIMENTAL RESULTS

To test the QTR performance, it was created 2 different scenarios: Scenario 1 (In-door environment to test only 3 Degrees of Freedom (DoFs), using a gyroscopic testbench [8]) and Scenario 2 (Out-door environment to test all 5 DoFs, to perform an eight shape path).

A. Scenario 1

The QTR was coupled to a gyroscopic test bench with 0 degrees of pitch and the setpoints of the Table I applied. The system behavior was compared to these values in Fig. 2.

This test shown on the Fig. 2 can be divided in 5 stages, which the first one have roll, pitch and yaw setpoints on 0 degrees, corresponding from 0 until 23 seconds. About yaw dynamics, the vehicle did not start aligned with the setpoint like the roll and pitch, but it is adjusted after 10 seconds.

TABLE I: Fast Control Allocation Algorithm

Time Stamp (sec)	**1**	**23**	**73**	**122**	**173**
ϕ (degrees)	0	30	0	-30	0
θ (degrees)	0	0	0	0	0
ψ (degrees)	0	100	0	-100	0
Propulsion (N)	10.3	10.3	10.3	10.3	10.3
$\hat{V}_x$ (N)	0	4.5	0	4.5	0

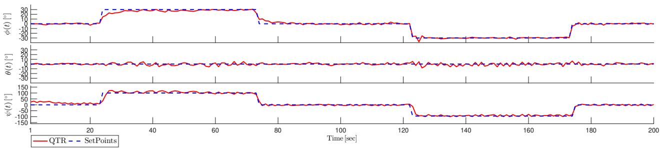

(a) Roll (ϕ), pitch (θ) and yaw (ψ) controlled responses

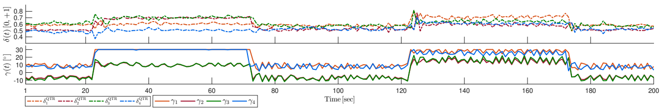

(b) QTR propulsion signals (δ_i) and servomotors tilting angles (γ_i)

Fig. 2: Controlled responses with QTR in a gyroscopic test bench for the setpoints shown in Table I

In the second stage, 30 degrees roll and 100 degrees yaw setpoints were inserted from 24 to 73 seconds. Pitch dynamics corrections were needed to keep it on 0 degrees. Fig. 2(b) shows that servomotors were inclined forward considerably, implying they were searching for the velocity setpoint.

In the third stage, from 74 to 122 seconds, setpoints came back to 0 to the linear velocity, roll, pitch and yaw dynamics.

In the fourth one, from 123 to 173 seconds, the same amplitudes but with inverted signals of the second stage were required. It can be notice some oscillations in the pitch control because those setpoints.

The last one (from 174 to 200 seconds) the setpoins reached the 0 values, as it was expected.

B. Scenario 2

It was tested in out-door environment, which the QTR elevates its height to 10 meters at the beginning.

After, it starts a trajectory like "8" format with linear velocity of 5 m/s reducing to 2.5 m/s in the two intersection moments. In the end, the QTR lands in the closest land point. This experimental test is followed in Fig. 3.

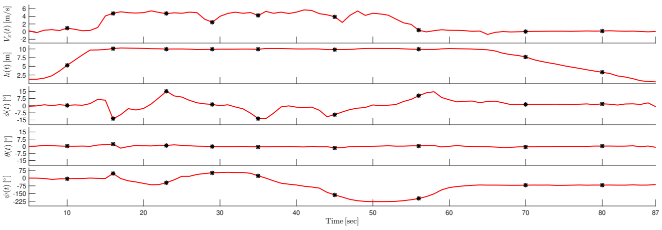

(a) Altitude (h), forward/backward velocity (V_x), roll (ϕ), pitch (θ) and yaw (ψ) controlled responses.

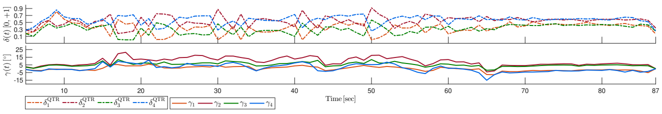

(b) QTR propulsion signals (δ_i) and servomotors tilting angles (γ_i)

Fig. 3: Controlled responses with the QTR in open field experimental test for "8" shape

Fig. 3 shows the controlled response along the time of the variables with its linear velocity, height and the state variables roll, pitch and yaw.

The ascent rate observed in Fig. 3 (b) is approximately 4 times faster than the descent rate as the previous scenario. The linear velocity was reduced in 29.5 seconds in the "8" intersection. The trajectory was executed close to 87 seconds.

VI. CONCLUSIONS

The objective of this work was based on those 6 stages:

- Projecting and develop the aircraft;
- Modelling of the kinematics and dynamics of it;
- Project, tuning and implementation of the control loops;
- Development of the proposed FCA;
- Perform tests in in-door environment (using the gyroscopic test bench);
- Perform tests in out-door environment.

According to the experimental test results to reach a reliable and stable QTR, the first step was successfully completed.

Modeling was essential for implementing and tuning controllers, leading to a more efficient allocation control method, which was necessary for the work to continue.

The control loop creation step was successful due to the tests, which showed that the control requirements were met.

The experimental tests proved through flights that QTR was reliable during the experiments, tracking the desired setpoint, for both scenarios.

FUTURE WORKS

The conclusion of this works opens different areas for future works. First, it is suggested to expand the FCA technique to other overactuated vehicles like a fixed-wing tilt rotor and an overactuated boat.

The second point is about analyzing the QTR performance in front of more allocation control subsystems. It will also serve as an important tool, this UAV can be used for exploring other areas, such as dam and power transmission line inspections [19], [20]

ACKNOWLEDGMENT

The authors would like to thank CEFET-MG and Leuphana University of Lüneburg for their financial support.

REFERENCES

[1] H. Menouar, I. Guvenc, K. Akkaya, A. S. Uluagac, A. Kadri, and A. Tuncer, "FAA drone registry tops one million," *Online*, vol. 55, no. 3, pp. 22–28, 2017.

[2] U. D. of Transportation, "UAV-enabled intelligent transportation systems for the smart city: Applications and challenges."

[3] A. Ryan, M. Zennaro, A. Howell, R. Sengupta, and J. Hedrick, "An overview of emerging results in cooperative UAV control," in *43rd Conference on Decision and Control (CDC) (IEEE Cat. No.04CH37601)*, vol. 1, 2004, pp. 602–607 Vol.1.

[4] J. Yang and J. Zhu, "A hybrid NDI control method for the high-alpha super-maneuver flight control," in *American Control Conference (ACC)*, 2016, pp. 6747–6753.

[5] Q. He, Y. Tan, X. Liu, Q. Jia, and J. Liu, "Reconfigurable nonlinear dynamic inversion for attitude control of a structurally damaged aircraft," *IEEE Access*, vol. 8, pp. 199 931–199 943, 2020.

[6] Y. Ziquan, Z. Youmin, and J. Bin, "PID-type fault-tolerant prescribed performance control of fixed-wing UAV," *Journal of Systems Engineering and Electronics*, vol. 32, no. 5, pp. 1053–1061, 2021.

[7] L. S. Rezende, A. M. Leite da Silva, and L. de Mello Honório, "Artificial immune system applied to the multi-stage transmission expansion planning," in *Artificial Immune Systems: 8th International Conference, ICARIS 2009, York, UK, August 9-12, 2009. Proceedings 8*. Springer, 2009, pp. 178–191.

[8] M. F. dos Santos, L. de Mello Honório, A. P. G. M. Moreira, P. A. N. Garcia, M. F. da Silva, and V. F. Vidal, "Analysis of a fast control allocation approach for nonlinear over-actuated systems," *ISA Transactions*, 2021. [Online]. Available: https://www.sciencedirect.com/science/article/pii/S0019057821004389

[9] M. F. dos Santos, L. de Mello Honório, A. P. G. M. Moreira, M. F. da Silva, and V. F. Vidal, "Fast real-time control allocation applied to over-actuated quadrotor tilt-rotor," *Journal of Intelligent & Robotic Systems*, 2021.

[10] M. F. da Silva, L. M. Honório, A. L. M. Marcato, V. F. Vidal, and M. F. Santos, "Unmanned aerial vehicle for transmission line inspection using an extended kalman filter with colored electromagnetic interference," vol. 100, 2020, pp. 322–333. [Online]. Available: https://www.sciencedirect.com/science/article/pii/S0019057819304872

[11] M. F. Pinto, L. M. Honório, A. Melo, and A. L. M. Marcato, "A robotic cognitive architecture for slope and dam inspections," *Sensors*, vol. 20, no. 16, p. 4579, 2020.

[12] R. W. Beard and T. W. McLain, *Small Unmanned Aircraft: Theory and Practice*, 2012, ISBN: 978-1-40084-060-1.

[13] G. J. Ducard, *Fault-tolerant flight control and guidance systems: Practical methods for small unmanned aerial vehicles*, 2009, ISBN: 978-1-84882-561-1.

[14] R. W. Beard, "Quadrotor dynamics and control."

[15] T. A. Johansen and T. I. Fossen, "Control allocation — a survey," *Automatica*, vol. 49, no. 5, pp. 1087–1103, 2013. [Online]. Available: https://www.sciencedirect.com/science/article/pii/S0005109813000368

[16] M. F. Santos, V. S. Pereira, A. C. Ribeiro, M. F. Silva, M. J. do Carmo, V. F. Vidal, L. M. Honório, A. S. Cerqueira, and E. J. Oliveira, "Simulation and comparison between a linear and nonlinear technique applied to altitude control in quadcopters," in *18th International Carpathian Control Conference (ICCC)*, May 2017, pp. 234–239.

[17] M. F. Silva, A. C. Ribeiro, M. F. Santos, M. J. Carmo, L. M. Honório, E. J. Oliveira, and V. F. Vidal, "Design of angular PID controllers for quadcopters built with low cost equipment," in *20th International Conference on System Theory, Control and Computing (ICSTCC)*, Oct 2016, pp. 216–221.

[18] R. W. Beard and T. W. McLain, *Small unmanned aircraft: Theory and practice*. Princeton university press, 2012.

[19] I. Z. Biundini, M. F. Pinto, A. G. Melo, A. L. M. Marcato, L. M. Honório, and M. J. R. Aguiar, "A framework for coverage path planning optimization based on point cloud for structural inspection," *Sensors*, vol. 21, no. 2, p. 570, 2021.

[20] A. G. Melo, M. F. Pinto, L. M. Honório, F. M. Dias, and J. E. N. Masson, "3D correspondence and point projection method for structures deformation analysis," *IEEE access*, vol. 8, pp. 177 823–177 836, 2020.